Research Square

Preprints are preliminary reports that have not undergone peer review.
They should not be considered conclusive, used to inform clinical practice,
or referenced by the media as validated information.

Sustainable Removal of U(VI) from Aqueous Solution Using PGB and Psg@FeNPs with Comparative Insights into Adsorption isotherms and Kinetics

Sandhya Chandrakar
University Teaching Department, CSVTU
Sangeeta Sahu
dr.sangeetasahu76@gmail.com
Bhilai Institute of Technology
Shilpa Sharma
Bhilai Institute of Technology
Madhurima Pandey
Bhilai Institute of Technology

Research Article

Keywords: Uranium, Psidium guajava, Iron nanoparticle, Comparative adsorption isotherm, Kinetics, Water contamination

Posted Date: June 4th, 2026

DOI: https://doi.org/10.21203/rs.3.rs-9781607/v1

License: This work is licensed under a Creative Commons Attribution 4.0 International License.
Read Full License

Additional Declarations: No competing interests reported.

Sustainable Removal of U(VI) from Aqueous Solution Using PGB and Psg@FeNPs with Comparative Insights into Adsorption isotherms and Kinetics

Sandhya Chandrakar[1], Sangeeta Sahu[2], Shilpa Sharma[3], Madhurima Pandey[4]

[1]Department of Applied Chemistry, University Teaching Department, CSVTU, Bhilai, Chhattisgarh, India

[2,3]Department of Engineering Chemistry, Bhilai Institute of Technology, Raipur, Kendri, New Raipur – 493661, Chhattisgarh, India

[4]Department of Engineering Chemistry, Bhilai Institute of Technology, Bhilai House, Durg 491001, CG, India

sandhyachandrakar1996@gmail.com

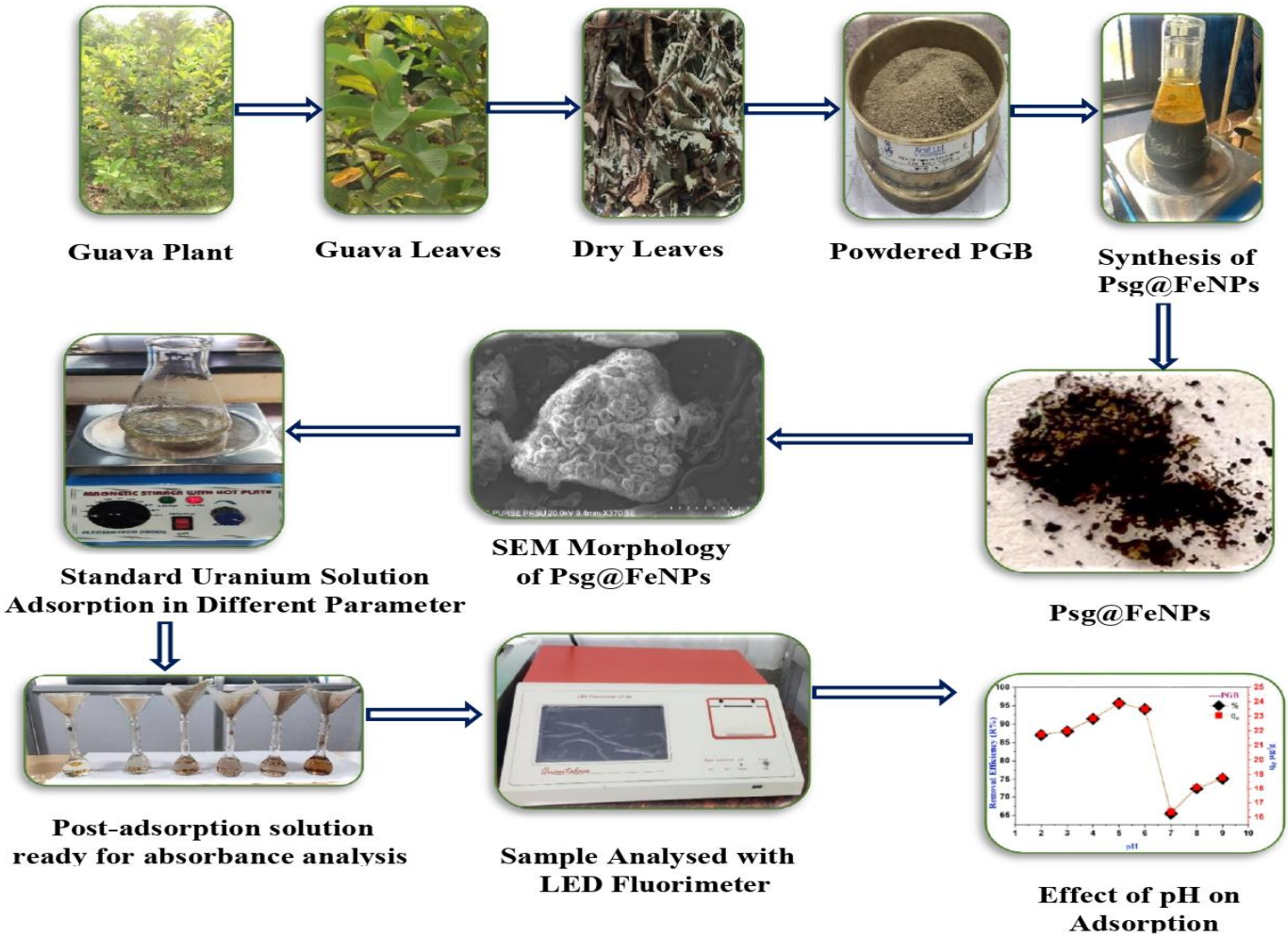
dr.sangeetasahu76@gmail.com

shilpa@bitraipur.ac.in

pandeymadhurima01@gmail.com

Abstract : *The present study investigates the elimination of U(VI) ions from aqueous medium using PGB (dried biomass) and Psg@FeNPs (Psidium guajava – mediated iron nanoparticles), with a comparative evaluation of their adsorption performance. The adsorbance were characterized by FTIR, XRD, and SEM, confirming the presence of functional groups responsible for uranium binding. Batch adsorption studies were conducted by optimizing parameters including pH, adsorbent dosage, contact time, and initial metal ion concentrations, with optimum conditions observed at pH 5 and 45 min. Under these conditions, a maximum adsorption efficiency of 94.05% was achieved. The Langmuir isotherms ($R^2 = 0.99$) best described the equilibrium data,suggesting monolayer adsorption, other than kinetic investigations used pseudo-second-order kinetics, indicating chemisorption as the dominant mechanism. Desorption and reusability studies further confirmed effective regeneration and stable performance over multiple cycle. Overall, both PGB and Psg@FeNPs exhibit strong potential as efficient and sustainable adsorbents for U(VI) removal from contaminated water.*

Graphical Abstract



Keywords: Uranium. Psidium guajava. Iron nanoparticle. Comparative adsorption isotherm. Kinetics. Water contamination.

Introduction

Technological advancement has significantly increased the demand for energy and its various sources, especially with the growing emphasis on protecting the environment from pollution. Traditional energy sources like coal and oil contribute heavily to environmental pollution, which has led to a shift toward chleaner alternatives such as nuclear energy. The use of nuclear energy has reduce dependence on coal and oil, thereby decreasing certain types of pollution[1]. However, nuclear energy also generates more hazardous waste, as it involve radioactive materials that remain active and potentially dangerous for extremely long periods. Nuclear processes produce liquid waste containing radioactive elements such as uranium and thorium, which must be carefully treated before disposal to prevent environment contamination [2,3]. Uranium is a naturally occurring omnipresent chemical element that belongs to the actinide series and its atomic number is 92. Uranium in nature is primarily consists of three isotopes ^{238}U, ^{235}U ,and ^{234}U with abundance of (99.724 %), (0.7%), and (0.0055%) respectively, and

each exhibiting long half-time[4]. Due to its chemical hazardous and radioactive properties, even at minimal concentrations, uranium poses significant environmental and health concerns.

Each year, substantial amounts of uranium-contaminated wastewater are generated, primarily as a result of various industrial and anthropogenic activities such as minig and milling. The nuclear industry is the largest contributor, where uranium is extensively used for energy production and the development of nuclear weapons. However other industries also contribute to uranium contamination, including the production of phosphate fertilizers, pigments, fossil fuels, catalysts, and more[4,5]. Uranium is a multivalent element that can naturally occur in the U(III), U(IV), U(V), and U(VI) oxidation state; however, in aqueous environments, the U(IV) and U(VI) states are most stable. Under reducing conditions, uranium predominantly exists as U(IV), which is relatively insoluble due to its tendency to form low-solubility minerals such as uraninite (UO_2). In contrast, in oxidizing environments, uranium is typically present as U(VI), a highly soluble form that exists primarily as the uranyl ion (UO_2^{2+}). This species readily forms a variety of aqueous complexes with constituents, especially hydroxide and carbonate, enhancing its mobility in natural waters [6]. In the disintegration process, the nuclear reactor releases an enormous quantity of radioactive isotopes and heavy toxic metals into the water [7]. The health of human and all other living things is seriously endangered by the high concentration of uranium and heavy hazardous sunstances discovered in the water bodies. The World Health Organization (WHO) recommends that the permitted amount of 30 μg/L for uranium in drinking water [8]. The kidneys, lungs, and even the nervous system are affected by uranium. The detrimental effects of uranium on the organs have been attributed to the complexes that for with phospholipids and proteins in cell. Severe health effects, including nephrotoxicity and cancer risk, may arise in the body system as consequence of the elevated uranium concentration[9].

Several separation techniques, such as electrochemical treatment, solvent extraction, ion-exchange, reverse osmosis, evaporation, membrane separation, flocculation, precipitation, and adsorption, are used in the elimination of uranium ions from the environment [10]. Among the various remediation techniques available for uranium removal, precipitation, solvent extraction, and adsorption are the widely studied and commonly applied. However, despite their popularity, precipitation and solvent extraction often face significant practical limitations. Precipitation relies on differences in solubility of uranium compounds in aqueous media and while effective, it lacks selectivity, is unsuitable for low-concentration solutions, and generates large volumes of alkaline sludge requiring extensive settling infrastructure. Solvent extraction involves transferring uranium ions between two or more immiscible phases, but it is hindered by low selectivity, emulsion formation, high solvent consumption, large volumes of organic waste, labor-intensive procedures, and the need for multi-stage processing to achieve effective recovery. These drawbacks have prompted increased interest in adsorption-based techniques, which offer greater simplicity, effeciency, and environmental compatibility [11,12].

Adsorption is the simplest and most widely used technique for removing toxic substances from water, as it is fast, easy to implement, and highly effective. However, conventional adsorbent materials often come with certain restriction, including expensive production expenses as well as limited adsorption capacity. To address these challenges, ongoing research is focused on developing sorbents that are more cost-effective, posessess higher adsorption efficiency, and are environmentally sustainable for the elimination of uranium and other hazardous heavy metals from untreated water.[13]. Within the realm of adsorption-based techniques, biosorption has gained considerable attention as a promising techniques for removing uranium, and other heavy metals from wastewater. Recognized for its cost-effectiveness and environmental sustainability, biosorption is considered a viable alternative to traditional remediation approaches. Naturally occurring residues, algae, microorganisms like bacteria,fungi, industrial and agricultural byproducts are all example of biosorbents. A vide range of plant derived biosorbent has been investigated [14-16]. In addition, substantial efforts have been devoted to developing advanced solid adsorbents with enhanced mechanical strenght, chemical stability, durability, selectivity, and adsorption performance. Nanostructured materials-such as bio-nanoparticles, carbon nanotubes, nanosheets, and nanofibers-have proven to be particularly intriguing alternatives due to their high surface area, exceptional adsorption capacity and selectivity under diverse conditions[17]. The large surface area, elevated reactivity, and occurence of numerous type of functional groups in nanobiosorbents are key factors underlying their strong adsorption capacity and enhanced interaction with target contaminants. The area of nanotechnology is expanding promptly and has many uses in different industries, because of their special qualities and possible benefits over bulk materials, nanoparticle production and application have attracted a lot of attention recently[18,19].

Nowadays, iron nanoparticles (INPs) are widely recognized as one of the most promising nanomaterials due to their unique physiochemical properties, including biocompatibility, ease of surface modification, and a high surface-to-volume ratio. This high ratio results in a significant number of surface atoms, enhancing their reactivity and making them highly effective in initiating and catalyzing various chemical reactions [20]. These properties have enabled their application across multiple fields such as biomedicine, food saftey, biosensing, environmental remediation, catalysis, magnetic data storage, and magnetic field-assisted seperation processes. To synthesize INPs, several conventional methods have been employed, including hydrothermal synthesis, sol-gel techniques, chemical co-precipitation, thermal decomposition, templet-assisted processes, vapour-phase methods, ultraviolet irradiation, aerosol-based approaches, and biological methods. However, to minimize toxicity and improve biocompatibility-particularly for biomedical and environmental uses- green synthesis strategies have gained considerable attention. Among these, plant-mediated synthesis offers a rapid, eco-friendly, and sustainable alternative for producing iron oxide nanoparticles with improved functional and safety profile [21-22].

The current work investigated the removal of uranium from aqueous solution using two adsorbents PGB (dried biomass) and Psg@FeNPs (Psidium guajava –mediated iron nanoparticles), which are synthesized from the guava plant *Psidium guajava* and compared their biosorption efficiency. After a preliminary test of several locally accesssible plants for their capacity to adsorb uranium from water, a prosective plant was chosen. In order to identify which of the two adsorbents utilized in this investigation was more effective, a comparative analysis was carried out. For the chosen adsorbent that shown higher uranium removal efficiency during the screening test, various factors affecting uranium adsorption such as pH, contact time, intial metal ion concentration, and adsorbent dose were examined. Isotherm, kinetic, and thermodynamics aspects were used to further explore the adsorption.

Experimental

Materials and Method

Chemicals

A 100 mg L^{-1} uranium stock solution (ICP-MS-66 N-0.01X-1 Uranium) was applied to make uranium solutions with varying concentrations. All the experiments involved analytical grade (AR) chemicals, specifically sodium hydroxide (NaOH), sodium pyrophosphate or tetrasodium pyrophosphate ($Na_4P_2O_7$), orthophosphoric acid (H_3PO_4), and nitric acid (HNO_3).

Collection and Preparation of the Biomass

After other locally accessible plants were first filtered out for this investigation, the guava plant, named Psidium guajava, was chosen. The prospective guava plant was gathered from the vicinity of Bhilai city in Chhatisgarh's Durg district. In Chhattisgarh and India, guava plants are found in several distinct regions in Figure 1. The leaf and twigs was collected from a mature plant of guava. The sample was cut into tiny pieces, steeped in boiling water for around 50 min, throughly cleaned under running water, and then left in distilled water for 4-5 hours. To get removal of the undesirable particles, the water was also changed 2-3 times. In order to soften the sorbent (Psidium guajava), this was done. Following a 15 – day drying period in the sun, they spent two days in a hot air oven at 55˚C. After being mashed up in a mixer, the dried biomass was filtered through 90 micron mesh. Psidium guajava biomass (PGB) was preserved in a sealed jar for the purpose of the testing in a sterile environment.



Fig. 1 Guava Plant (Psidium guajava) used in the present study

Pre-leaching of biomass

The leaching of biomass, PGB powder (≤ 90 micron) was pre-treated with an equal volume (1:1) solution of hydrochloric acid (HCl) for 1 hour. The leached material was passed via Whatman filter paper No.42, and the retained biomass was repeatedly cleaned with double distilled water until the filtrate becme neutral pH. The neutralized biomass was subsequently dried at 50 ℃ in a hot air oven for approximately 12 hours.

Green route synthesis of Iron Nanoparticles (Psg@FeNPs)

A green route synthesis method for nanoparticles was employed using only a metal salt (as a precursor) and a green substrate (serving as the reducing agent). Several reactions conditions-including precursor and reducing agent concentrations, temperature, pH, and reaction time-were carefully adjusted to obtained desirable nanoparticle for various applicatons. Iron nanoparticles were synthesized by hydrolizing an aqueous solution of iron salt and NaOH at room temperature under atmospheric conditions. The Psg@FeNPs nanoparticle were synthesized by mixing the rection components and continuously stirring the solution on a magnetic stirrer for 7 hours to facilitate uniform nycleation and controlled growth of the nanoparticles [23]. In the present investigation, 0.1 M of $FeSO_4.7H_2O$ iron salt as a precursor, and Psidium guajava biomass (PGB) was employed as a green reducing/stabilizing agent, aiding in the dispersion of nanoparticles and limiting their agglomeration, thereby reducing the mean particle size. The use of 0.1 M of NaOH as the precipitating agent led to the immediate appearance of a black precipitate, confirming the synthesis of iron nanoparticles. The reaction proceeds rapidly with a high yield, and magnetite crystals form immediately upon the addition of the precipitating agent to the iron salt solution[24]. The synthesis of Psg@FeNPs nanoparticles may proceed via the following Figure 2.

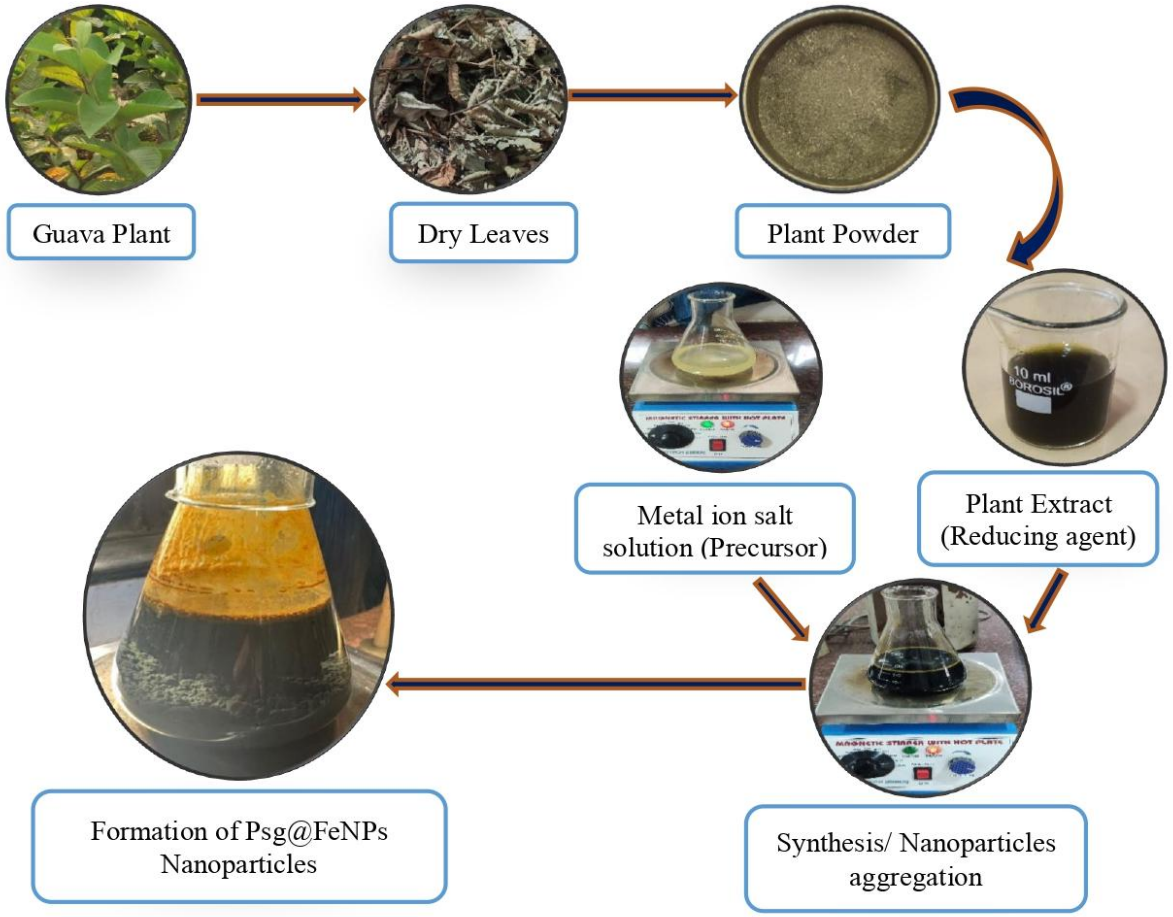


Fig 2. Schematic diagram of green synthesis of Psg@FeNPs using Guava leaves extract.

Instrumental analysis

Elemental composition and surface morphology of the Psg@FeNPs were examined using Energy Dispersive X-Ray (EDX) spectroscopy and Field Emission Scanning Electron Microscopy (FE-SEM) at the laboratories of IIT Bhilai, Chhattisgarh, Kindia. Functional group analysis of the nanopartilce surface was performed using Fourier Transform infrared Spectroscopy (FTIR)x- over the spectral range of 4000-400 cm^{-1}. FTIR spectra were recorded using a Bruker OPUS-7.5.18 spectrophotometer at the NCNR, Pt. Ravishankar Shukla University, Raipur (C.G.). The crystallographic structure of the Psg@FeNPs nanoadsorbents was investigated via X-ray Diffraction (XRD) using a D8 advance diffractometer. XRD analysis was conducted within a 2θ range of 10 ˚to 100 ˚confirm the phase composition and crystalline nature of the sample. The concentration of the uranium in the solution was determined using a QUNATALASE LED Fluorimeter (Model LF-2a).

Optimization of adsorption conditions

The adsorption behaviour of two adsorbents, PGB and Psg@FeNPs for the removal of uranium was syntematically investigated through batch mode adsorption investigations the tests were carried out by varying the adsorbent dose (0.1 g to 1.0 g for PGB in 50 mL volume and 0.001

g to 0.014 g for Psg@FeNPs in 25 mL volume), initial U(VI) concentration (10 ppb or µg/L to 100 µg/L), pH (2 to 9), and contact time (5 to 120 minutes), utilizing a magnetic stirrer operated at room temperature to determine the optimum adsorption parameters. The solution was filtered using Whatmann filter paper no. 42 following the prescribed contact time. Using an LED fluorimeter, the remaining concentrations of U(VI) in the filtrate was then calculated. It is widely recognize for its high accuracy and reliability in quantifying uranium in aqueous solutions, with the capability to detect trace concentrations as low as 0.1 µg/L [25]. By calculating the difference between the initial and final uranium concentrations in the aqueous solution, the amount of uranium adsorbed by the biosorbent was determined. The removal efficiency R (%), adsorption capacity q_e (µg/g), and distribution coefficient K (L/g) of PGB and Psg@FeNPs Were determined using equations (1), (2) and (3):

Removal efficiency,

$$R\,\% = \frac{(C_i - C_f)}{C_i} \times 100 \qquad (1)$$

Adsorption capacity,

$$q_e = \frac{(C_i - C_f)}{M} \times V \qquad (2)$$

Distribution coefficient,

$$K = \frac{(C_i - C_f)}{C_f} \times \frac{V}{M} \qquad (3)$$

where M is the amount of adsorbent utilized (g), V is the volume of solution (L), and C_i and C_f are the initial and final U(VI) ion concentration in solution (µg/L), respectively[26].

Quality assessment and validation

A standard uranium stock solution (100 mg/L, ICP-MS-66 N-0.01X-1 uranium) was employed for experimental procedures and instrument calibration. Uranium solutions of varying concentrations were preparaed using standard laboratory equipement, including micropipettes and an analytical balance. To minimize matrix effects, the standard addition method was applied. Each measurement was performed in triplicate, and the average of four reading was recorded. Only those results exhibiting a standard deviation within ± 10 % were considered acceptable. All analysis were conducted at a constant tempreture in a pristine, clean environment to ensure accuracy and reliability.

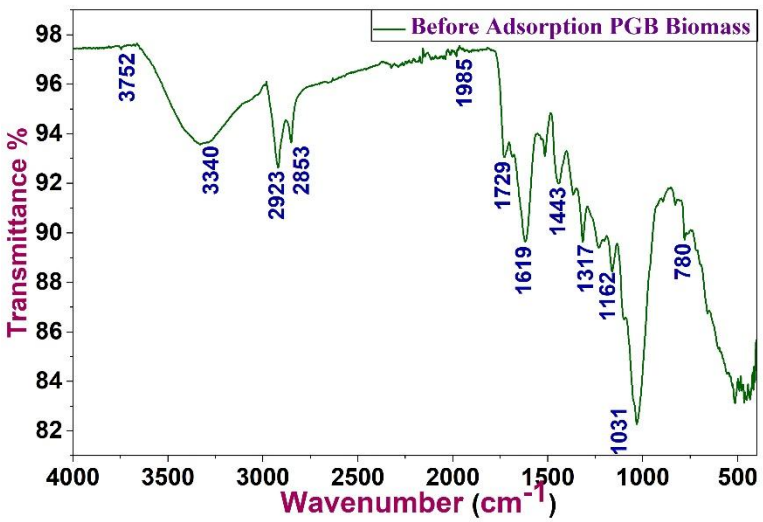
Result and discussion

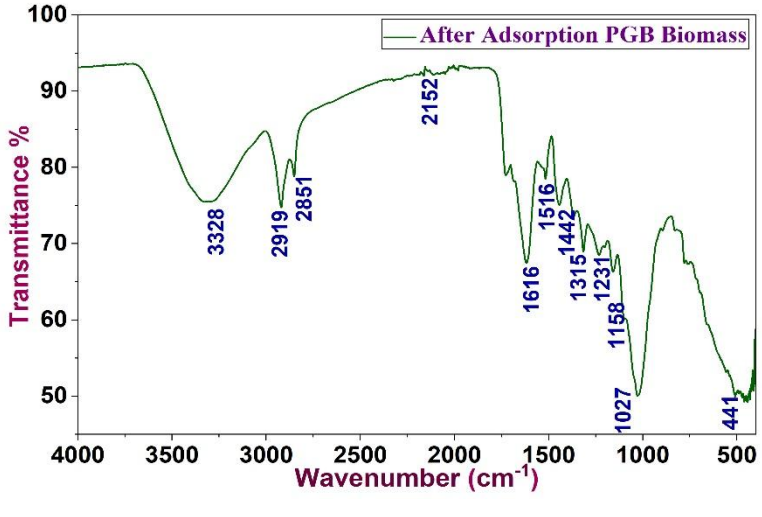
Characterization analysis of PGB biomass and Psg@FeNPs

Infrared study of PGB bbiomass and Psg@FeNPs

FTIR spectra of PGB biomass and Psg@FeNPs in Figure (3 a,b,c,d)were detected in the mid – infrared range (4000 – 500 cm^{-1}) before and after adsorption to elucidate the involvement of surface functional groups in the binding process. For pristine PGB biomass, the wide band seen at 3340 cm^{-1} is indicative of hydroxyl groups O – H stretching vibrations, which slightly shifted to 3328 cm^{-1} after adsorption, indicating their participation in U(VI) ion interaction. The peaks at 2923 and 2853 cm^{-1} (C – H stretching) showed minor shifts to 2919 and 2851 cm^{-1}, respectively. The characteristics band at 1619 cm^{-1} attributed to C=O or aromatic C=C stretching was shifted marginally, while the peaks at 1317 and 1162 cm^{-1} (C-N/C-O streatching) also exhibited slight displacement after adsorpiton. Notably, the band around 1031 cm^{-1} shifted to 1027 cm^{-1} , confirming the involvement of alcohol and carboxyl groups in U(VI) binding. Additionally, the appearance/intensification of low-frequency band near 441 cm^{-1} suggests possible U – O bond formation [27,28]. In the case of Psg@FeNPs, the broad O – H stretching band shifted from 3324 cm^{-1} to 3126 cm^{-1} after adsorption, representing stronger interaction compared to raw biomass. The C – H stretching peaks at 2918 and 2848 cm^{-1} showed slight variations, while the band at 1618 cm^{-1} (C=O stretching) shifted to 1605 cm^{-1}, reflecting coordination with the adsorbate. The peaks at 1316 and 1160 cm^{-1} were displaced to 1343 and 1132 cm^{-1}, respectively, suggesting the active role of amine and hydroxyl groups in uranium complexation. Importantly, distinct bands appeared at 885 and 788 cm^{-1} along with a prominent band around 591 cm^{-1}, which is associated to Fe – O vibrations and possible U – O – Fe coordination, confirming prospering uranium immobilazation on the nanoparticle composite [29,30].

Comparative FTIR analysis confirm that both PGB biomass and Psg@FeNPs exhibit spectral shifts after U(VI) adsorption, indicating the involvement of hydroxyl, carboxyl, and amine functional groups in uranium binding. In PGB, only slight displacements of the O – H and C=O bands were observed, suggesting surface complexation of U(VI) through oxygen – containig groups. In contrast, Psg@FeNPs showed more pronounced peak shifts aong with distinct





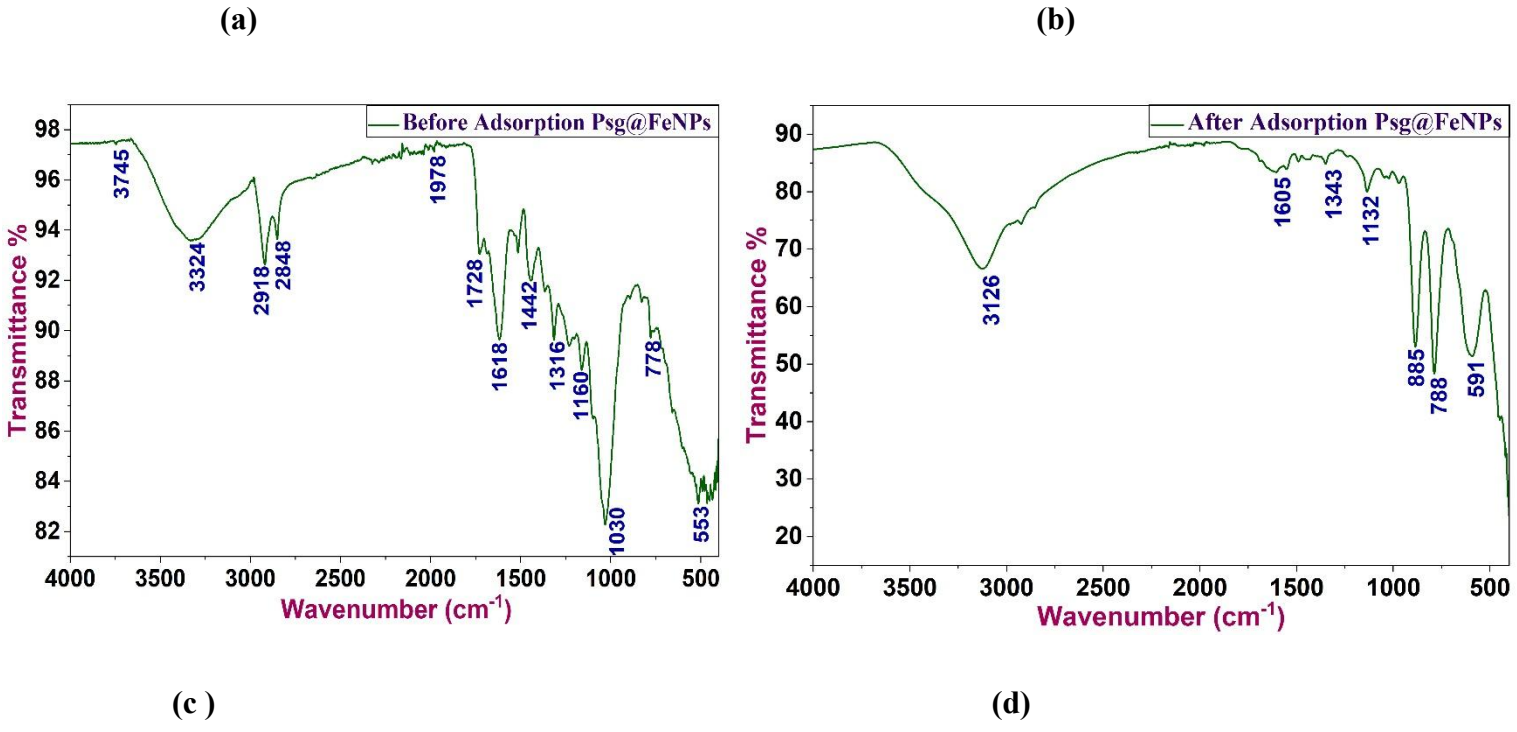


Fig. 3 a, b, c, and d FTIR spectrum of PGB biomass and Psg@FeNPs, a and b represents PGB biomass spectrum before and after uranium adsorption, c and d represents Psg@FeNPs spectrum before and after uranium adsorption

SEM analysis of PGB bbiomass and Psg@FeNPs

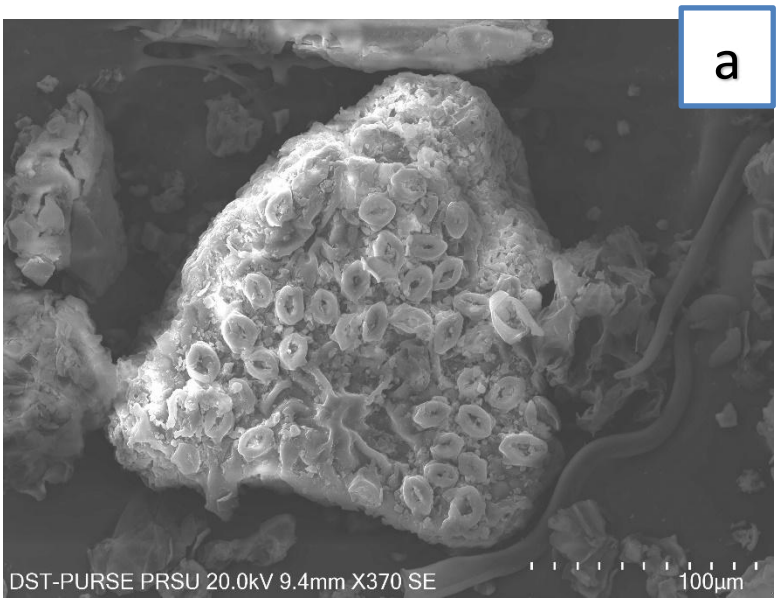
The surface morphology of PGB biomass previous and post uranium (VI) adsorption was investigated using Scanning Electron Microscopy (SEM). The micrograph of the pristine biomass Figure 4 a exhibits an irregular, fibrous, and heterogenous architechture with layered structures, grooves, and natural cavities. The rough surface texture and presence of microvoids indicates the availability of abundant active sites, which facilitate the intention and immobilization of uranium species. After exposure to U(VI) ion in Figure 4 b significant morphological modifications are observed. The biomass surface appears comparitively compact and partially covered with granular and aggregated deposits. Several previously distinct cavities and surface irregularities become less prominent, suggesting pore filing and surface coverage by adsorbed uranium. The clustered particulates observed on the surface confirm the succesful binding and accumulation of uranyl ions (UO_2^{2+}) onto the biomass matrix. These structural alterations amy be attributed to surface complexation, electrostatic attraction, and ion – exchange interactions between U(VI) species and oxygen – containing functional groups present in biomass. The evident morphological transformation strongly substantiates the effective biosorption of uranium onto PGB biomass [31,32]

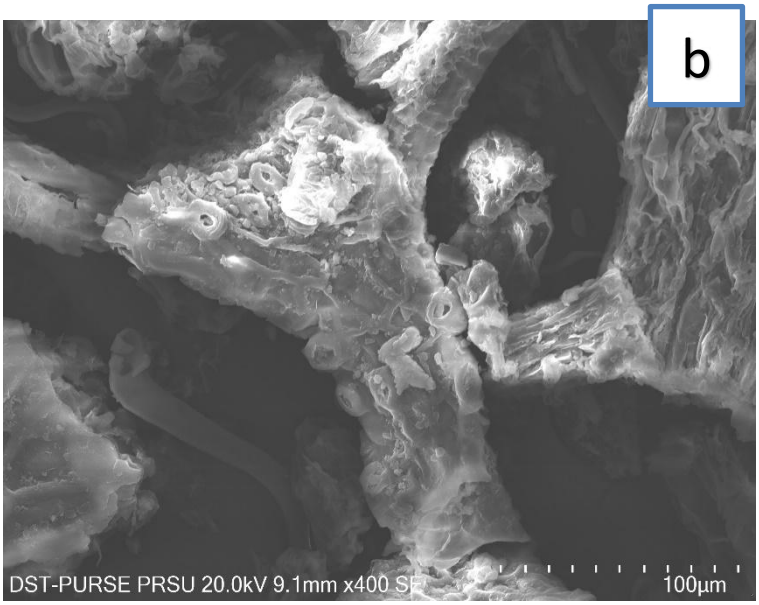
The SEM micrograph of pristine Psg@FeNPs and U(VI) adsorbed Psg@FeNPs in Figure 4 c and d clearly demonstrate the alteration in surface morphology following uranium adsorption. As observed in Figure 4 c, the pristine Psg@FeNPs exhibit an irrregular and heterogenous

architecture composed of agglomerated particles with sharp crystalline features and distinct inter – particle voids, indicating a rough and highly textured surface. In contrast, Figure 4 d reavels significant structural modification after exposure to uranium (VI). The nanoparticle surface appears comparatively more compact and densely coated with fine granular and rod – like deposits, resulting in partial masking of cavities and a noticiable reduction in visible void spaces. The enhanced aggregation and formation of clustered surface layers suggests the successful immobilization of uranyl ions (UO_2^{2+}) onto the Psg@FeNPs matrix. This morphological transformation indicates that uranium binidng occurs predominantly through surface complexation and coordination interactions with functional groups present on Psg@FeNPs, leading to surface coverage and structural reaarangement, subsequently verifying the synthetic nanocomposites efficient adsorption capacity.

Energy – dispersive X – ray spectroscopy (EDS) analysis

Energy Dispersive X – ray (EDX) spectroscopy was used to analyze the elemental composition of Psg@FeNPs both before and after uranium adsorption (Figure 5). The EDX spectrum of the as – synthesized Psg@FeNPs (Figure 5 a) confirms the presence of C, O, S, Fe, and Au elements indicating the formation of iron oxide nanoparticles supported on a carbonaceous matrix. Fe and O are observed as the major constituents, corresponding to the Fe – O framework of the nanocomposite, while Au is attributed to supper coating during analysis. After the adsorption experiments (Figure 5 b), the EDX spectrum displaya an additional uranium (U) signal, which was absent in the initial samole. The appearance of this uranium peak in the post adsorption spectrum clearly evidence the successful binding and accumulation of U(VI) onto the Psg@FeNPs surface. The retention of Fe and O signals alongside the uranium peak further suggests that the structural integrity of the nanocomposite remains preserved during the adsorption process. Thus, EDX ananysis confirm the effective immobilization of uranium by Psg@FeNPs [33].





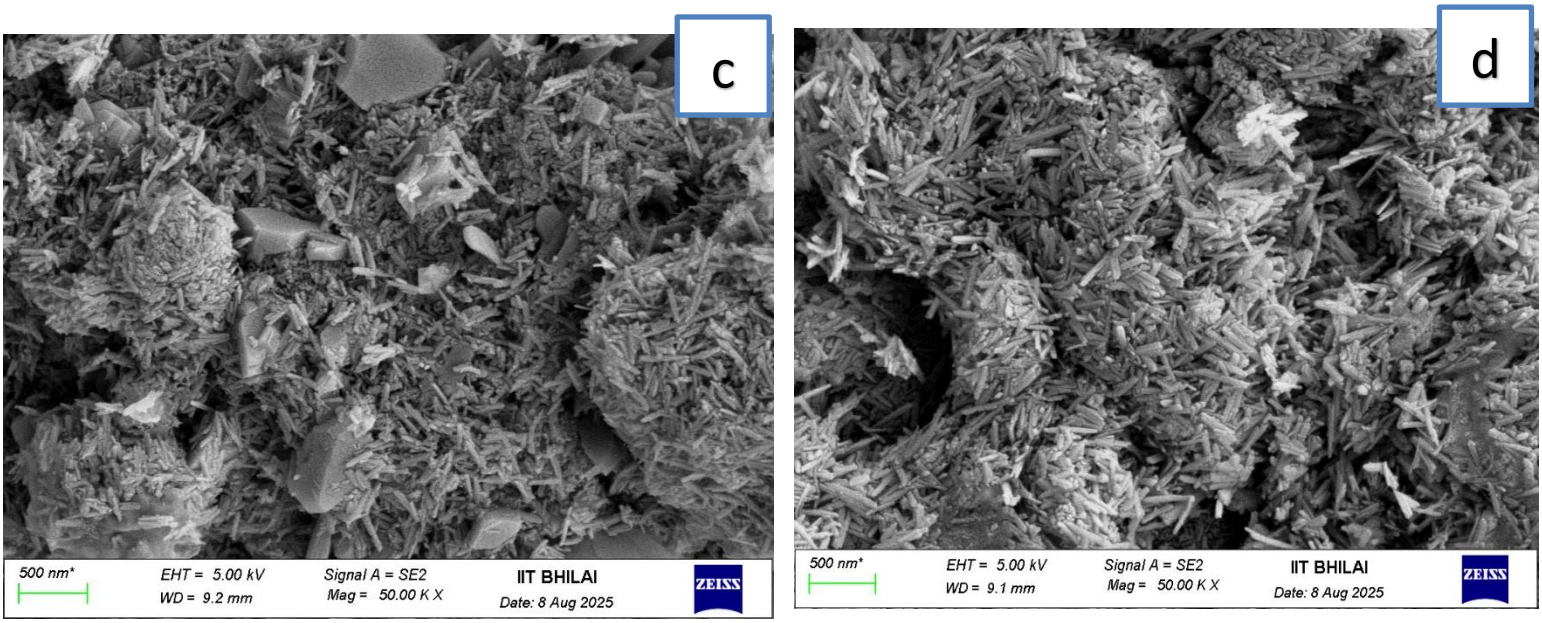


Fig. 4 (a – d) SEM morphology of PGB biomass and Psg@FeNPs, a and b represents SEM images of PGB biomass before and after uranium (VI) adsorption, c and d represents the SEM images Psg@FeNPs before and after urnaium (VI) adsorption

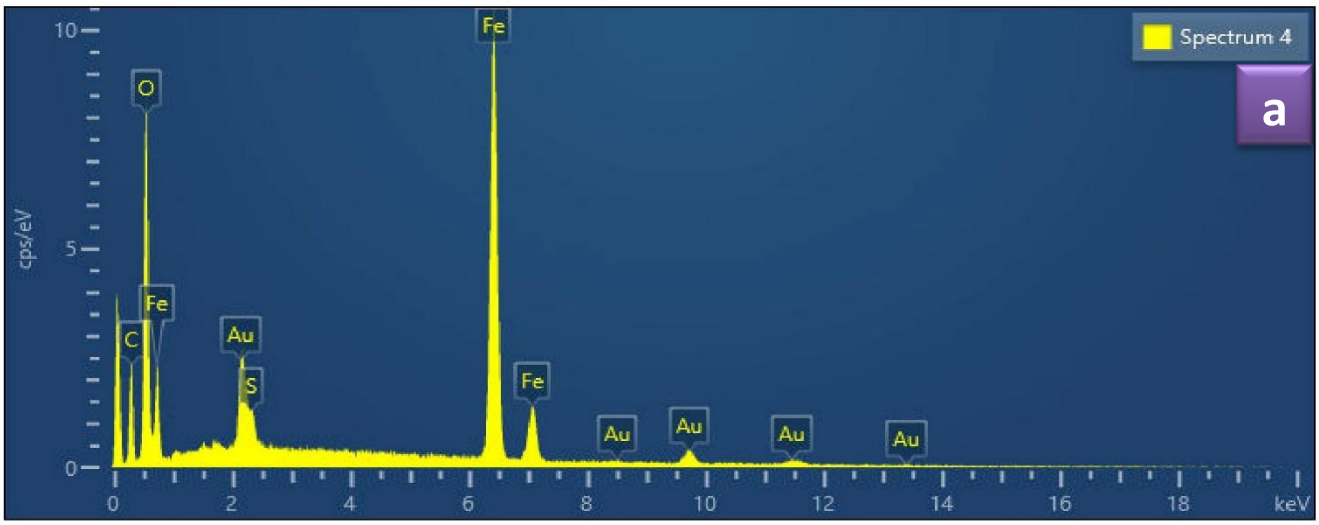
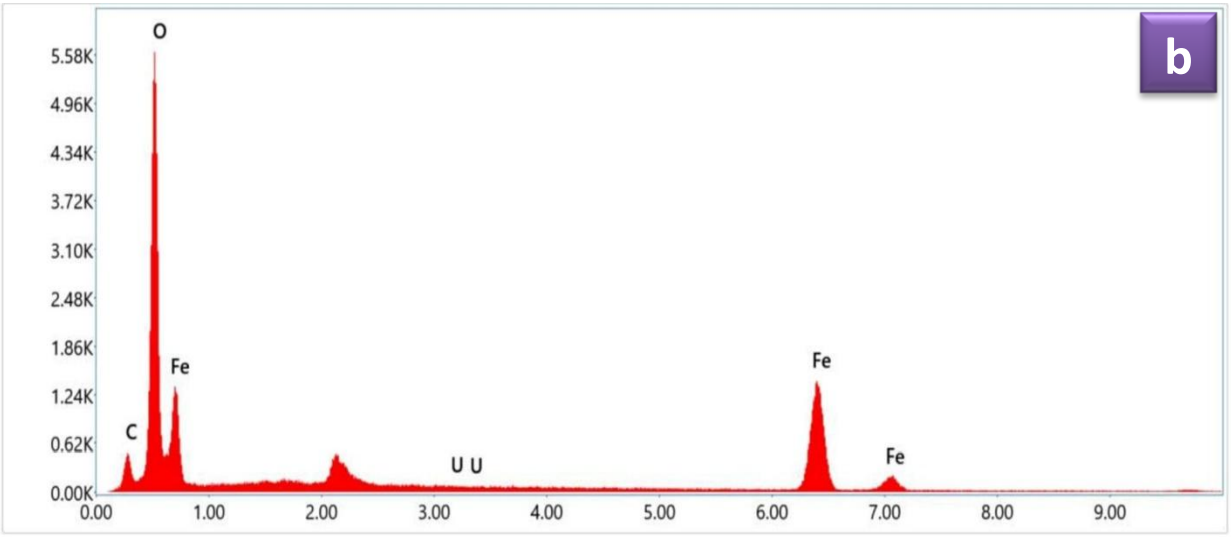


Fig. 5 (a, b) EDX spectra of Psg@FeNPs before and after uranium (VI) adsorption, respectively



XRD analysis of Psg@FeNPs

X – ray diffraction (XRD) analysis was employed to investigate the crystalline nature and phase distribution of the synthesized of Psg@FeNPs within a range of 10˚ - 100˚(Figure 6). The diffraction profile revealed prominent peaks at approximately 2θ values near 30˚, 35˚, 43˚, 57˚, and 62˚, attribited to the (220), (311), (400), (511), and (440) lattice planes of Fe – based nanoparticles. These diffractiom peaks are consistent with the standard JCPDS card No. 85-1436, confirming the successful formation of crystalline iron nanoparticles in the synthesized material. Among the observed reflections, the most intense diffraction peak was recorded at around 2θ ≈ 35.57˚, which is indexed to the (311) plane and indicating the predominant crystalline orientation of the iron nanoparticles. The sharp diffraction peaks observed in the XRD pattern reflect good crystallinity of the synthesized nanoparticles and indicates negligible impurity phases. The average crystalline size was determined by applying the Debye – Scherrer equation:

$$D = \frac{k\,\lambda}{\beta \cos\theta} \qquad (4)$$

Here, D represents the mean crystalline size, k is the dimensionless Scherrer constant (0.9), λ is the wavelenght of Cu – Kα radiation (0.15406 nm), β signifies the peak broadenning expressed as is the full width at half maximum (FWHM), and θ is the corresponding Bragg angle. Using the most intense diffraction peak at 2θ ≈ 35.57˚, the average crystalline size of the

synthesized PSg@FeNPs nanoparticles was caluclated to be approximately 27 nm, confirming the nanocrystalline nature of the prepared material.

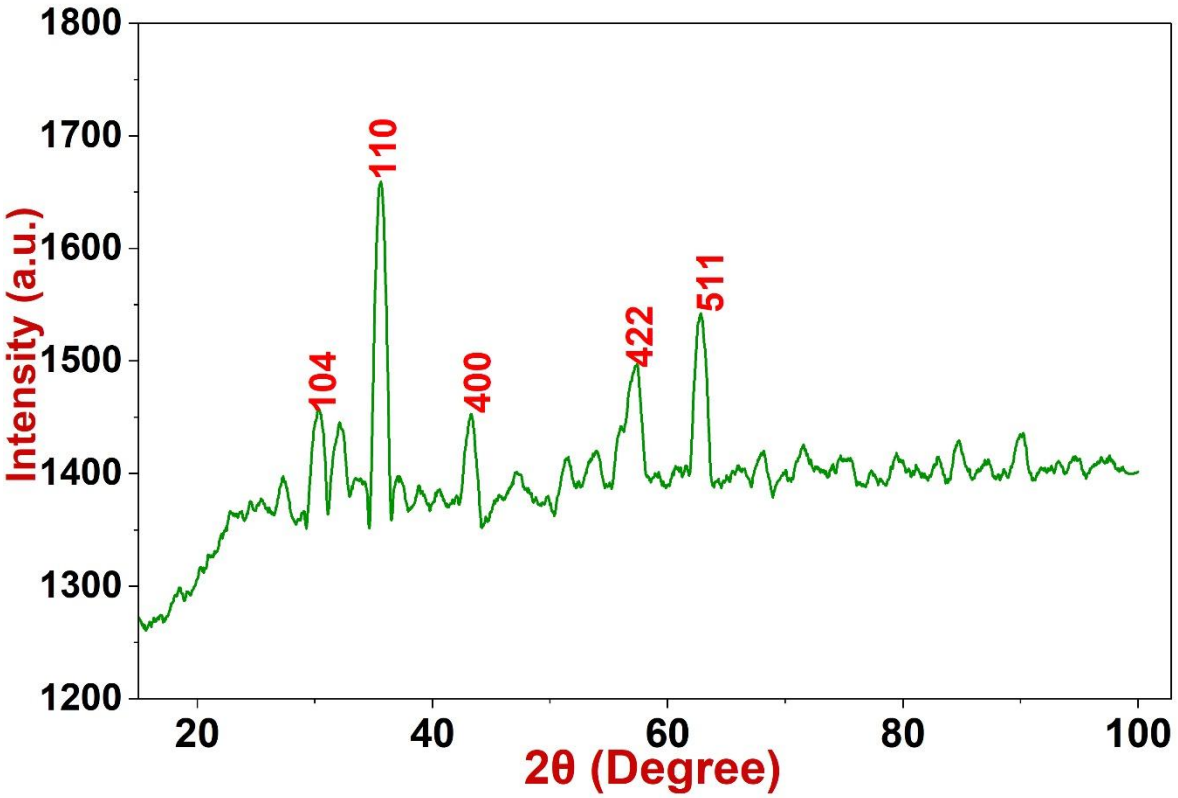


Fig. 6 XRD peaks of Psg@FeNPs

Evaluation of adsorption potential

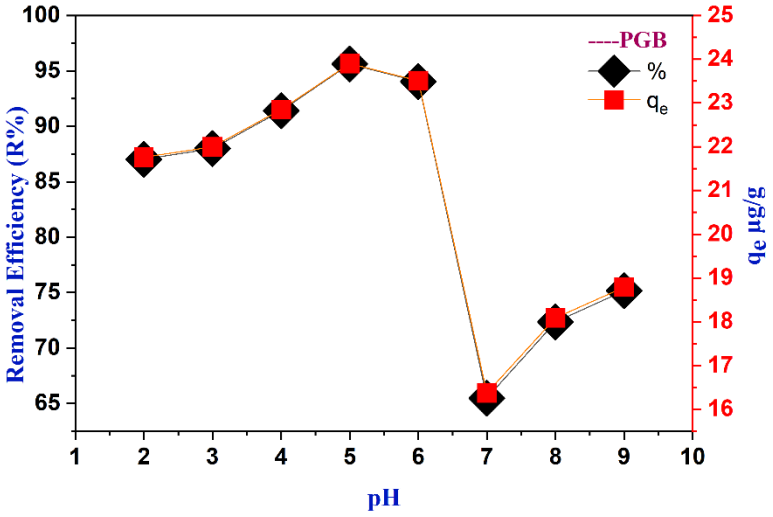
Effect of pH on the adsorption

pH is an important factor in adsorption processes, as it governs metal ion speciation and solubility while also altering the surface charge and interaction properties of the adsorbent [34]. The effect of pH on U(VI) adsorption onto PGB and Psg@FeNPs was investigated over the range of 2 – 9. The pH was regulated using 0.1 M NaOH and 0.1 M HNO_3 and The corresponding results are depicted in Figure 7. As shown in Figure 7 (a,b) the maximum biosorption capacities of PGB and Pgs@FeNPs were 23.90 µg/g and 547.12 µg/g, respectively. The corresponding removal efficiencies were 95.51 % and 87.54 %, both achieved ar Ph 5. In the case of PGB, a sharp deep was observed at neutral pH (i.e., pH 7), followed by a slight increase with further rise in pH, suggesting the formation of complexes with carbonates and hydroxyl ions. Whereas, for Psg@FeNPs, uranium uptake by the adsorbent improved progressively with pH, attaining its optimum at pH 5. However, beyond pH 5, a continuous decreased.Under mildly acidic conditions, uranyl ions readily form complexes with inorganic anions such as F^- and SO_4^{2-}. In contrast, under neutral to alkaline conditions, they tend to form

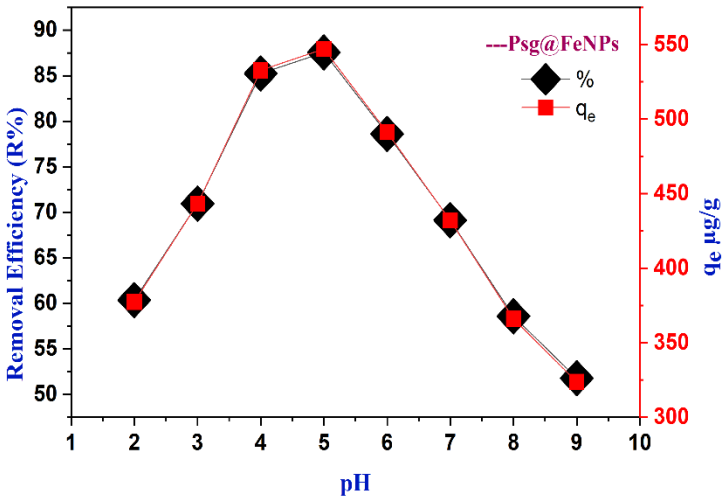
anionic complexes with CO_3^{2-} and OH^-. When the solution pH is maintained between 2 to 9, a majority of the dissolved U(VI) exists as complexed or hydrolyzed species, including $UO_2(OH)^+$, $(UO_2)_2(OH)_2^{2+}$, and $(UO_2)_3(OH)_5^+$ [35]. An increase in U(VI) removal was observed with rising solution pH for both PGB and Psg@FeNPs, with optimal removal achieved at pH 5. Beyond this point, the removal efficincy gradually decreased. With decreaing pH, the solubility of U(VI) increases, enhancing its tendency to interact with negatively charged functional groups present on the surface of the biosorbents, leading to complex formation at lower pH levels [36].

Effect of contact time on adsorption

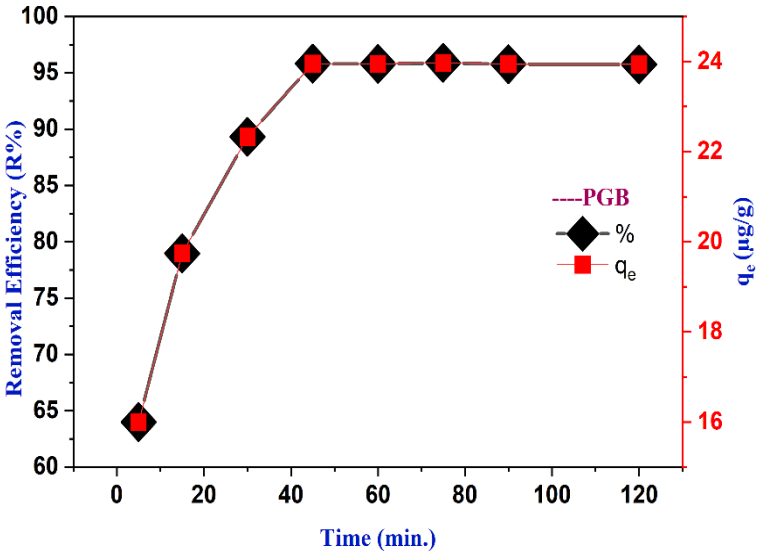
Contact time significantly influences chemical and biological processes, particularly in biosorption. The equillibrium time is especially important, as it represents the point at which most avilable active sites on the adsorbent are occupied by metal ions, and maximum adsorption efficiency is achieved [37]. The impact of contact time on U(VI) biosorption was investigated over a time range of 5-120 minutes. For this purpose, 0.1 g of PGB and 0.002 g of Psg@FeNPs were separately added to uranium solutions with a concentration of 50 µg/L. the pH of the solution was maintained at 5 for both biosorbents throughtout the experiment. The impact of contact time on the biosorption process is shown in Figure 7 (c, d). U(VI) removal efficiency increased progressively with contact time, attaining equilibrium at 45 min for both biosorbents. The adsorption capacity remained constant beyond this point, indicating that the available active sites on the biosorbent surfaces had become saturated. The rapid attainment of equilibrium suggests a high affinity of both PGB and Psg@FeNPs for U(VI), and that most of the adsorption occurred at the early stage, attributed to the high availability of unoccupied active sites on the adsorbent. After 45 minutes, the reduced rate of adsorption can be atrributed to the decreased availability of these active site, resulting in minimal further uptake[38].



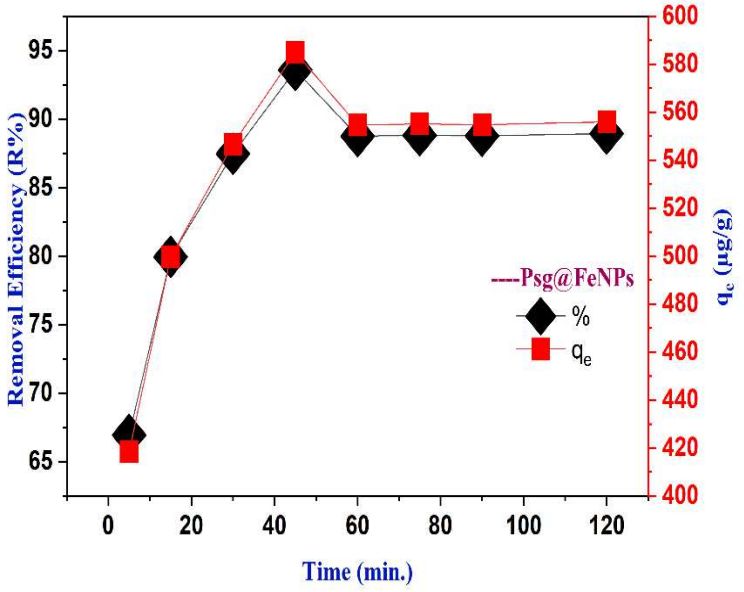
(a)



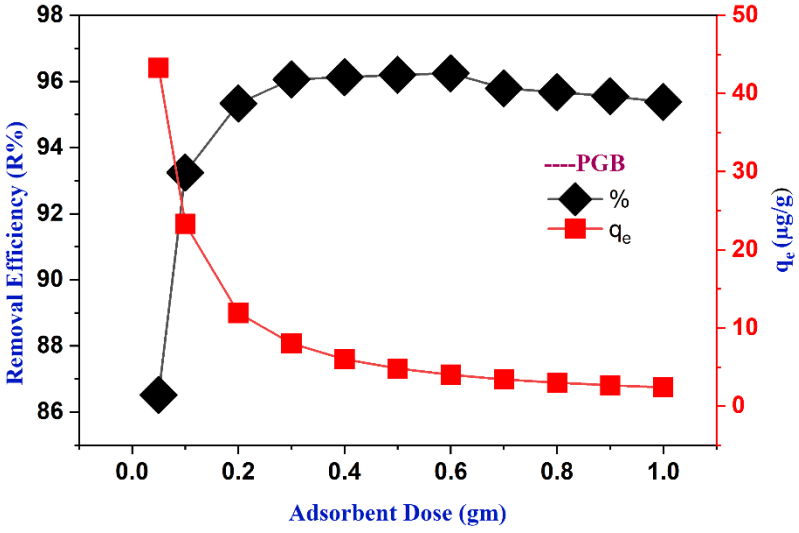
(b)


Removal Efficiency (R%)
qe (µg/g)
Time (min.)
----PGB
%
qe

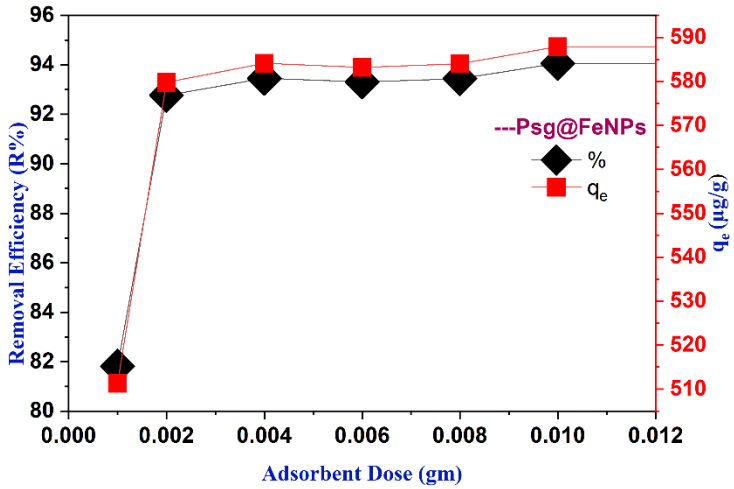
(c)


Removal Efficiency (R%)
qe (µg/g)
Time (min.)
----Psg@FeNPs
%
qe

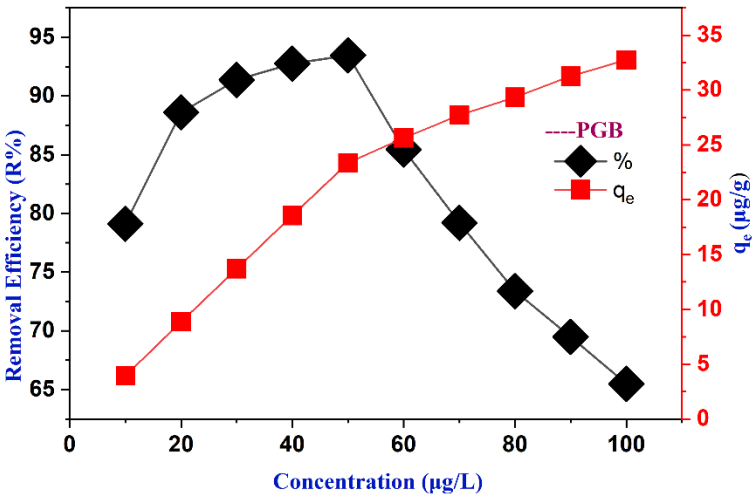
(d)

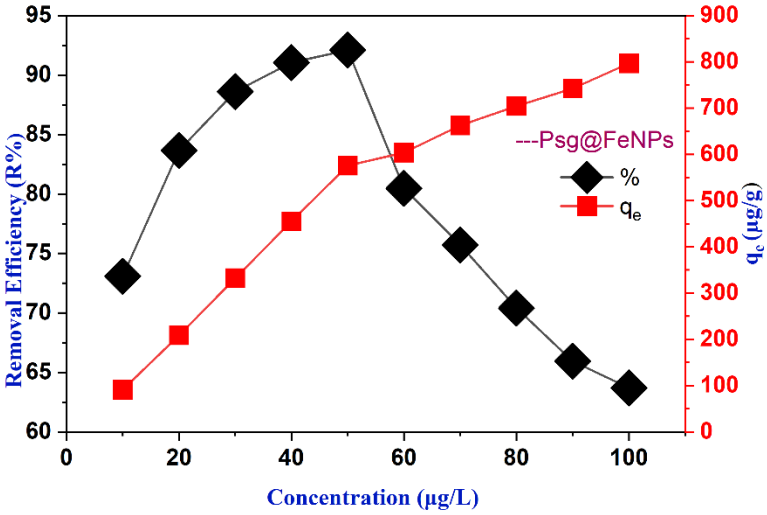

Removal Efficiency (R%)
qe (µg/g)
Adsorbent Dose (gm)
----PGB
%
qe

(e)


Removal Efficiency (R%)
qe (µg/g)
Adsorbent Dose (gm)
---Psg@FeNPs
%
qe

(f)


Removal Efficiency (R%)
qe (µg/g)
Concentration (µg/L)
----PGB
%
qe


Removal Efficiency (R%)
qe (µg/g)
Concentration (µg/L)
---Psg@FeNPs
%
qe

(g) **(h)**

Fig. 7 (a – h). Batch adsorption studies for U(VI) removal by PGB biomass and Psg@FeNPs: (a, b) effect of pH, (c, d) effect of contact time, (e, f) effect of adsorbent dose, and (g, h) effect of initial metal ion concentration

Effect of adsorbent dosage on adsorption

Sorbent dosage is a crucial factor that significantly affects the adsorption performance, as it determines the total number of available active sites for uranium (VI) ion binding on the sorbent surface. To assess this effect a series of batch adsorption process were carried out using varying amounts of PGB (0.1 to 1.0 g) and Psg@FeNPs (0.001 to 0.016 g). Throughout the study, other parameters such as solution pH and contact time was held constant to ensure that variations in adsorption efficiency were soley due to variations in sorbent dose. Increasing the sorbent generally enhances the availability of binding sites, thereby improving the uptake of uranium (VI) until saturation is achieved. Figure 7 (e, f) illustrates the correlation between biosorption capacity (q_e) and percentage removal (R%) as a function of PGB and Psg@FeNPs dosage. In case of PGB, an increase in sorbent dosage resulted in a gradual drecreases in biosorption capacity while the percentage removal (R%) continued to increase. This inverse relationship occurs because, at higher dosages, the available uranium (VI) ions become insufficient to fully saturate the increased number of binding sites, leading to lower uptake per unit mass of biosorbent. Additionally, at elevated biomass concentrations, particle aggregation and overlapping of active sites may occur surface area and assesibility of functional groups for metal binding [39,40]. In contrast, for Psg@FeNPs, both biosorption capacity and percentage removal nearly constant beyond the dosage of 0.002 g. this indicates that the active sites on the nanoparticles surface reach saturation quickly attributed to their high surface area and reactivity. Further increases in nanoparticles dosage do not significanlty contribute to additional uranium (VI) removal, because of the saturation of available metal ions in solution and the agglomeration of nanoparticles at higher concentrations [41].

Effect of initial ion concentration on adsorption

All experimental conditions were maintained constant, while the initial concentration of U(VI) ions was varied in the range of 10 µg/L to 100 µg/L to evaluate its influence on the adsorption behaviour. The result of initial metal ion concentration on the adsorption performance of PGB was shown in Figure 7 (g). As the initial concentration increased, the biosorption capapcity (q_e) consistently increased from 3.95 to 32.75 µg/g. This is due to the increased mass transfer driving force at higher concentrations, promoting greater interactoin between U(VI) ions and active sites on the biosrbent. In contrast removal efficiency initially increased, reaching a maximum of approximately 93.5 % at 50 µg/L, but then declined with further increse in U(VI) concentration. The decrese in % removal at higher concentration indicates that active sites on

the biomass become saturated and the fixed biosorbent does cannot accommodate the excess uranium ions. Following the trend observed with PGB, a similar pattern was noted for Psg@FeNPs as shown in Figure 7 (h). As the initial U(VI) concentraton increased, the biosorption capacity (q_e) increased significantly from 91.35 to 796.32 µg/g. indicating enhanced loading ions on the nanoparticles surface. However, the removal efficiency exhibited a peak at 92.08% around 50 µg/L, beyond which it gradually declined. The high biosorption capapcity at increasing U(VI) concentrations reflects the strong affinity of Psg@FeNPs for uranium ions, demonstrating their excellent potential for efficient uptake even at elevated concentrations.

Adsorption isotherm models

Aa a standard approach in adsorption studies, equilibrium isotherm models are commonly employed to evaluate the sorption capacity and to elucidate the interaction behaviour of the adsorbent – adsorbate systems. These model contribute to a better understanding of the adsorption mechanism, surface characteristics of the adsorbent, and its affinity for the adsorbate at equlibrium [42]. To investigate the adsorption mechanism and equilibrium charateristics, the experimental data were fitted to Langmuir, Freundlich, and Temkin isotherm models.

Langmuir isotherm

The Langmuir isotherm is based on the concept of monolayer coverage, where each adsorbate molecule is associated with a single adsorption site on the surface. It further presumes that the surface of the adsorbent is homogenous, where all adsorption sites possess equal energy and possessing uniform adsorption potential [43]. The linear expression of the Langmuir isotherm model is represented in Eq 5.

$$\frac{C_e}{q_e} = \frac{1}{bQ_0} + \frac{C_e}{Q_0} \qquad (5)$$

Here q_e denotes the amount of adsorbate adsorbed at equilibrium per unit mass of biosorbent (µg g^{-1}), C_e is the equilibrium concentration in aquesous phase (µg L^{-1}), Q_0 is corresponds to the maximum monolayer adsorption capacity (µg g^{-1}), and b is the Langmuir affinity constant (Lµg^{-1}). The linear plots of C_e against C_e/C_q for both PGB and Psg@FeNPs shown in Figure 8 (a, b) yielded high correlation coefficients of 0.995 and 0.990, respectively, suggesting a significant conformity of the experimental data with Langmuir isotherm model. This suggests monolayer adsorption of U(VI) ions onto a homogeneous surface. The Langmuir constants Q_0 and b, representing the maximum adsosorption capacity and the affinity of binding sites, respectively, were evaluated using the slope and intercept of the linearized plots, as

summarized in table 1. The maximum monolayer adsorption capacity obtained from the Langmuir model was 34.834 µg g^{-1} for PGB and 833.33 µg g^{-1} for Psg@FeNPs.

The separation factor or equilibrium parameter (R_L), a key indicator of the Langmuir isother, was calculated using Eq 6.

$$R_{L=} \frac{1}{1 + b\, C_i} \qquad (6)$$

where b is the Langmuir constant (L μg^{-1}) and C_i is the initial uranium concentration (µg L^{-1}). If $R_L = 0$ isotherm is irreversible, linear if $R_L = 1$, unfavourable if $R_L > 1$ or favourable $0 < R_L < 1$.

For both PGB and Psg@FeNPs, the R_L values within the range of 0 – 1 suggest that the adsorption of U(VI) onto both adsorbents. The reduction in R_L values with increasing initial uranium concentrations confirms that the adsorption process becomes more favorable at higher concentrations.

Freundlich isotherm

The Freundlich isotherm described adsorption on a heterogeneous surface with sites possessing different affinities and energies. It assumes a heterogenous distribution of adsorption heat and allows for interactions between adsorbed molecules. The model is mathematically expressed as Eq 7.

$$Q_e = K_f \times C_e^{\frac{1}{n}} \qquad (7)$$

The logirithmic equation being :

$$\ln q_e = \ln K_f + \frac{1}{n} \ln C_e \qquad (8)$$

Here K_f denotes the Freundlich constant associated with adsorption capacity, while n reflects the intensity of adsorption. The apllicability of the Freundlich isotherm was assessed by ploting $\ln q_e$ versus $\ln C_e$, as shown in Figure 8 (c, d). based on the linear form of Eq 8. The parameters K_f and n were determined from the intercept and slope of the linearized plot, respectively, and are presented in table 1. The Freundlich constant n indicates provides insight into the adsorption mechanism; n=1 represents linear adsorption, while n<1 is associated with chemisorption and n > 1 signifies physical adsorption. In the present study, the slope (1/n) values for PGB and Psg@FeNPs are 0.2497 and 0.2556, respectively, corresponding to n values of 4.004 and 3.913. Since both values are grater than 1, the adsorption process for both biosorbents is characterized as physical adsorption [44]. Additionally, the Freundlich constant K_f, which reflects the adsorption capacity, was abserved to be 13.944 for PGB and significantly higher at 317.394 for Psg@FeNPs, suggesting a much greater adsorption capacity in the case of nanoparticles. Furthermore, the correlation coefficients (R^2) for the linearized Freundlich plots were 0.8027

for PGB and 0.7715 for Psg@FeNPs, indicating a good agreement between the model and the experimental data.

Temkin isotherm

The heat involved in the sorption process was evaluated using the Temkin isotherm model, where the parameter b_T (J/mol) represents the heat of adsorption. This parameter was calculated based on Eq. 9 and is illustrated in the linear plot shown in Figure 8 (e, f) According to the Temkin iostherm, adsorption energy decreases linearly as surface coverage increases, owing to interactions between the adsorbate and adsorbent[45].

$$q_e = \left(\frac{RT}{b_T}\right) ln\,(A_T) + \left(\frac{RT}{b_T}\right) ln\,(C_e) \qquad (9)$$

Where Temkin's binding constant A_T (L/ µg) reflects the equilibrium binding strength and its associated with the maximum adsorption energy, thus provinding insight into the adsorption potential. The heat of the biosorption process is represented by b (J/mol), where T represents the absolute temperature in Kelvin (K), while R is the universal gas constant (8.314 $Jmol^{-1}K^{-1}$)[46]. The Temkin constants (A_T and b) were derived from the linear plot of q_e versus ln $C_{e.,}$ and the obtained parameters are summarized in table 1. According to obtained data the adsorption behaviour was interpreted using the Temkin isotherm model, which assumes a linear reduction in heat of adsorption with increasing surface coverage due to adsorbate – adsorbent interactions. For the PGB, the heat of adsorption b was calculated as 5.7693 J/mol, and the Temkin binding constant K_T was found to be 8.49 µg/g, indicating moderate binding affinity. In comparison, the Psg@FeNPs exhibited a much higher b value of 142.53 J/mol, with a corresponding K_T of 6.38 µg/g, reflecting stronger interactions and slightly lower equilibrium binding strength. The Temkin isotherm plats demonstrated a strong correlation with the experimental results, with R^2 values of 0.8802 for PGB and 0.8456 for nanoparticles, suggesting a reasonably good fit of the model to both systems.

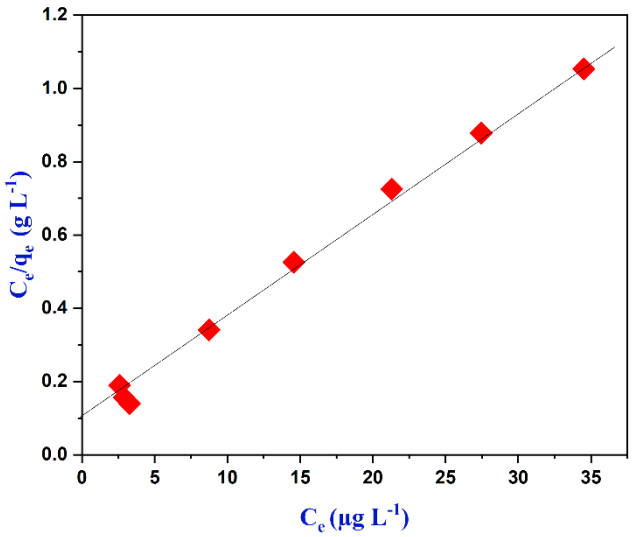
Among the evaluated isotherm models, the Langmuir model exhibited the best fit for both PGB and Psg@FeNPs, as it exhibited highest correlation coefficients (R^2), suggesting monolayer adsorption on a heterogenous surface while the Freundlich and Temkin models also showed a reasonably good fit, their lower R^2 values suggest that Langmuir is more appropriate for describing the uranium adsoption behavior in this study.

Table 1. Isothem model parameters and correlation coefficients (R^2) for uranium adsorption onto PGB and Psg@FeNPs using Langmuir, Freundlich and Temkin isotherms.

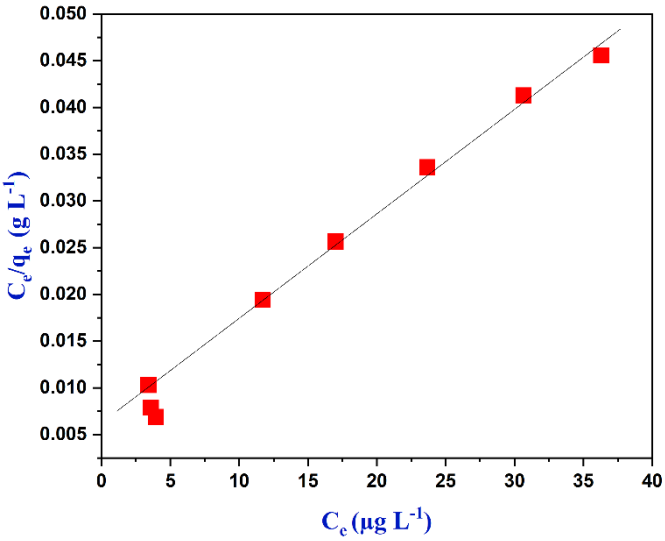
Langmuir's model			Freundlich's model			Temkin's model		
b (L μg^{-1})	Q_0 (µg g^{-1})	R^2	K_f(µg g^{-1})/(µg L^{-1})	n	R^2	A_T (L μg^{-1})	b_T (J/mol)	R^2
PGB								

0.3298	34.843	0.995	13.944	0.249	0.8027	8.491	5.769	0.880
Psg@FeNPs								
0.2553	833.33	0.99	314.394	0.255	0.771	6.380	142.53	0.845

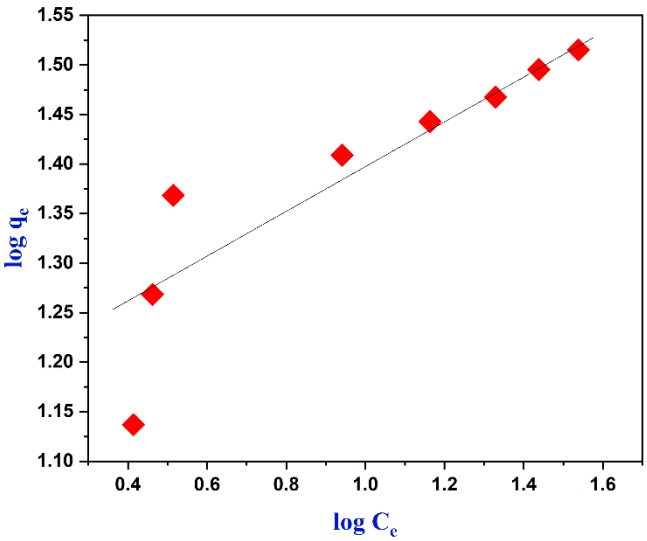
(a)



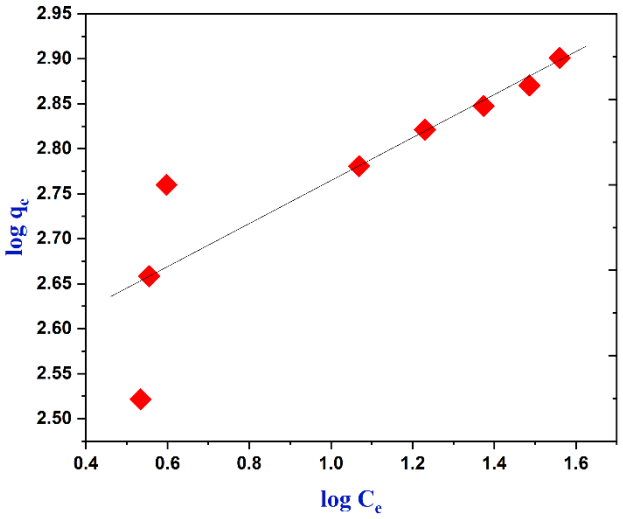
(b)



(c)



(d)



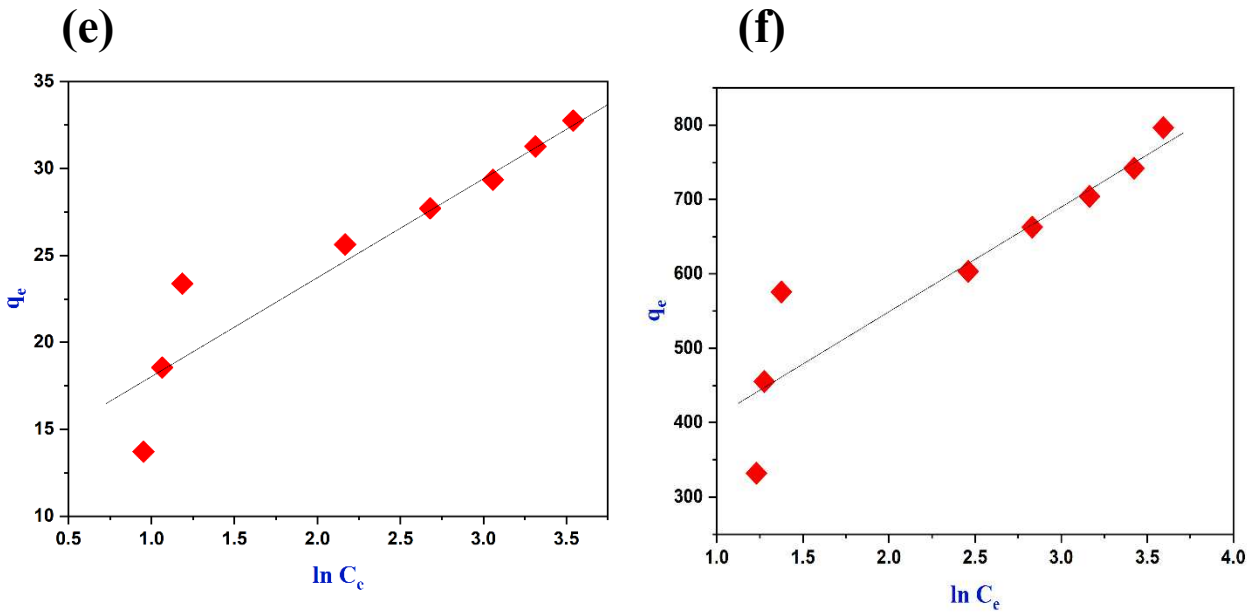


Fig. 8 (a – f) Isotherm modelling studies of U(VI) adsorption onto PGB biomass and Psg@FeNPs: (a, b) Langmuir isotherm plots, (c, d) Freundlich isotherm plots, and (e, f) Temkin isotherm plots for PGB biomass and Psg@FeNPs, respectively

Kinetics

The adsorption kinetics elucidate the rate and mechanism of interaction between metal ions and the adsorbent surface, thereby governing the time required to reach equilibrium and shedding light on the underlying adsorption mechanism. Typically, three key processes occur at the solid – liquid interface,where external mass transfer occurs through the bulk and film diffusion, intraparticle diffusion, and surface adsorption interactions. To elucidate the biosorption mechanism in greater detail, the kinetic data were analyzed sing three commonly applied models, including the pseudo-first-order (Lagergren) model, the pseudo-second-order model, and the intraparticle diffusion model proposed by Weber and Morris. The pseudo first order kinetic model suggests that the rate of adsorption depends mainly on the availibility of vacant adsorption sites on the adsorbent surface. In contrast, according to the pseudo second order kinetic model, the adsorption rate is governed by both the number of available active sites and the concentration of U(VI) ions in solution. The mathematical expressions governing these models are presented below [47-49] :

Pseudo – first order model : $ln(q_e - q_t) = lnq_e - k_1 . t$ (10)

Pseudo second order model : $\frac{t}{q_t} = \frac{1}{k_2 q_e^2} + \frac{1}{q_e} . 1$ (11)

Intraparticle diffusion model : $q_t = k_{int} . t^{\frac{1}{2}} + C$ (12)

In this context, q_e and q_t corresponds to the adsorption capacities and at time t, respectively (µg g^{-1}). The rate constants k_1 (min^{-1}) and k_2 (g µ$g^{-1}min^{-1}$) represents the pseudo first order and

pseudo second order kinetics, respectively. The intraparticle diffusion constant k_{int}, has units of ($\mu g\ g^{-1}$. $Min^{-1/2}$) C denotes the boundary layer thickness parameter $\mu g\ g^{-1}$.

Comparison of the three kinetic models indicated that the pseudo second order model best descrives the adsorption behaviour for both adsorbents, as indicated by the highest correlation coefficients (R^2). The adsorption parameters were determined by plotting t/q_t against time (t), thereby confirming the suitability of this model for describing the adsorption behaviour. For PGB, the R^2 value was 0.9995 with a calculated equilibrium adsorption capacity (q_e) of 24.63 µg/g, closely matching the experimental q_e of 23.93 µg/g. the corresponding rate constant (k_2) was found to be 0.01555 g/(µg.min). similarly, for Psg@FeNPs, the pseudo – second – order model demonstrated good agreement with experimental results, yielding an R^2 of 0.9992, a theoretical q_e of 555.56 µg/g, and an experimental q_e of 555.96 µg/g. the rate constant k_2 in this case was 0.00191 g/(µg.min). A summary of these kinetic parameter is presented in table 2. The intraparticle diffusion model showed partial fitting, implying that while intraparticle diffusion is involved the adsorption mechanism, it is not the sole rate – determinig – step. This is further supported by the relatively lower correlation coefficients, with R^2 values of 0.7533 for PGB and 0.5775 for Psg@FeNPs. This results confirm that the adsorption of U(VI) onto both PGB and Psg@FeNPs follows pseudo second order kinetics, indicating chemisorption involving valency forces or elctron exchange as the predominant mechnism.

Table 2. Psuedo second order parameters for removal of U(VI) on PGB and Psg@FeNPs.

Adsorbents	**k g/(µg.min)**	**q_e(µg/g)**	**R^2**
PGB	0.01555	24.630	0.9995
Psg@FeNPs	0.00191	555.56	0.9992

Desorption :

The desorption performance of U(VI) from Psg@FeNPs was systematically evaluated using 0.1 M HCl and 0.1 M EDTA through five successive adsorption – desorption cycles. Both eluents exhibited comparable initial desorption efficiencies (~88 %), confirming their effectiveness in removing surface – bound U(VI) ions. However, a pronounced difference was observed in their reusability behaviour. In the case of HCl, the desorption efficiency declined sharply from 87.98% to 47.71%, indicating significant loss of active adsorption sites. This decline is largely due to the protonation of surface functional groups (-OH and $–COO^-$) and possible structural deterioration of Psg@FeNPs under strongly acidic conditions, which adversely affects the integrity of the adsorbent.

In contrast, EDTA demonstrated a relatively gradual decrease in desorption efficiency from 88.47% to 65.35%, suggesting improved stability and retention functional groups over repeated

cycles. The superior performance of EDTA is governed by its Chelation mechanism, which facilitates the formation of stable, soluble complexes with U(VI) ions, thereby enabling efficient desorption without significantly altering the structural framework of Psg@FeNPs. Consequently, the adsorbent maintains higher reusability and performance consistency. Overall, while HCl is effective for initial desorption, EDTA is a more suitable and sustainable eluting agent for repeated adsorption – desorption applications.

Conclusion : Efficient removal of uranium from contaminated water remains a critical concern for environmental sustainability. In this study, PGB and Psg@FeNPs were effectively utilized as eco – friendly adsorbents for U(VI) removal, achieving a maximum adsorption efficiency of 94.05% under optimized conditions. The experimental data were fitted to Freundlich, Langmuir, and Temkin isotherm models, with the Langmuir model exhibitng the highest correlation coefficient ($R^2 \approx 0.99$), consistent with monolayer adsorption on a homogenous surface. Kinetic studies revealed that the adsorption process follows pseudo – second – order behaviour, indicating chemisorption as the rate – limiting mechanism. Desorption and reusability studies revealed high initial recovery, with the Chelation – based system exhibitng a higher desorption efficiency of ~88.47% along with improved stability over successive cycles compared to acidic conditions, indicating better preservation of active sites and enhanced regeneration performance. Overall both PGB and Psg@FeNPs demonstrate strong potential as efficient, sustainable, and regenrable material for uranium remediation in aquesous environments. Compared to conventional treatment methods, the present approach offers advantages such as simplicity, eco – friendliness, and effecxtive regenatration, highlighting its suitability for practical wastewater treatment applications.

References:

1. Ahmad, Ahmad A. "Kinetics of uranium adsorption from sulfate medium by a commercial anion exchanger modified with quinoline and silicate." *Journal of Radioanalytical and Nuclear Chemistry* 324 (2020): 1387-1403.
2. Mahmoud, Mohamed Ahmed. "Sorption of U (VI) ions from aqueous solution by eggplant leaves: Isotherm, kinetics and thermodynamics studies." *Progress in Nuclear Energy* 138 (2021): 103829.
3. Yousef, Lamia A. "Recovery of uranium (VI) from sulfate leach liquor using modified duolite." *Zeitschrift für anorganische und allgemeine Chemie* 646.7 (2020): 340-353.
4. Smječanin, Narcisa, et al. "Study of uranium biosorption process in aqueous solution by red beet peel." *Journal of radioanalytical and nuclear chemistry* 331.3 (2022): 1459-1471.
5. Liaska, Aikaterini, Panagiotis Tsamos, and Fotini Noli. "Uranium removal from aqueous solutions onto biochar and irradiated sewage sludge." *Journal of Radioanalytical and Nuclear Chemistry* (2025): 1-11.
6. Xie, Yi, et al. "Emerging natural and tailored materials for uranium-contaminated water treatment and environmental remediation." *Progress in materials science* 103 (2019): 180-234.

7. Deshmukh, Poonam, et al. "Magnetite based green bio composite for uranium exclusion from aqueous solution." *Journal of Radioanalytical and Nuclear Chemistry* 332.2 (2023): 297-310.
8. Geneva, Switzerland. "Guidelines for drinking-water quality." *World Health Organization: Geneva, Switzerland* (2011).
9. Bayramoglu, Gulay, et al. "Uranium sorption by native and nitrilotriacetate-modified Bangia atropurpurea biomass: kinetics and thermodynamics." *Journal of applied phycology* 30 (2018): 649-661.
10. Abd El-Magied, Mahmoud O., et al. "Removal of uranium ions from contaminated solutions by adsorption on cerium and lanthanum magnesium ferrite." *Journal of Radioanalytical and Nuclear Chemistry* 334.1 (2025): 1049-1066.
11. Ibrahim, Mohamed M., et al. "A facile and cost-effective adsorbent derived from industrial iron-making slag for uranium removal." *Journal of Radioanalytical and Nuclear Chemistry* 329.3 (2021): 1291-1300.
12. Abd El-Magied, Mahmoud O., et al. "Uranium removal from aqueous medium using Co 0.5 Mn 0.5 Fe 2 O 4 nanoparticles." *Journal of Radioanalytical and Nuclear Chemistry* 327 (2021): 745-753.
13. Tan, Lichao, et al. "Synthesis of Fe3O4@ TiO2 core–shell magnetic composites for highly efficient sorption of uranium (VI)." *Colloids and surfaces A: Physicochemical and engineering aspects* 469 (2015): 279-286.
14. Alharbi, Khalid N., et al. "Investigation of adsorption isotherms and thermodynamic models of uranium biosorption from aqueous solutions by Rumex Acetosella." *Journal of Radioanalytical and Nuclear Chemistry* 334.3 (2025): 2251-2270.
15. Chen, Can, Jun Hu, and Jianlong Wang. "Biosorption of uranium by immobilized Saccharomyces cerevisiae." *Journal of Environmental Radioactivity* 213 (2020): 106158.
16. Liu, Yun, Antonio Serrano, and Denys Villa-Gomez. "Biological treatment of mine-impacted waters on the context of metal recovery." *The Future of Effluent Treatment Plants* (2021): 499-522.
17. Chandrakar, Sandhya, et al. "A Review on the Efficiency of Adsorbents for Uranium Pollutant Remediation from Wastewater." *Transactions of the Indian Institute of Metals* 78.2 (2025): 55.
18. El-Maghrabi, Heba H., et al. "Magnetically modified hydroxyapatite nanoparticles for the removal of uranium (VI): Preparation, characterization and adsorption optimization." *Journal of hazardous materials* 378 (2019): 120703.
19. Bayramoglu, Gulay, and Mehmet Yakup Arica. "Agmatine ligand functionalized magnetic alginate beads for removal of U (VI) ions from solution." *Journal of Radioanalytical and Nuclear Chemistry* 333.8 (2024): 4197-4210.
20. Ebrahiminezhad, Alireza, et al. "Green synthesis and characterization of zero-valent iron nanoparticles using stinging nettle (Urtica dioica) leaf extract." *Green Processing and Synthesis* 6.5 (2017): 469-475.
21. Beheshtkhoo, Nasrin, et al. "Green synthesis of iron oxide nanoparticles by aqueous leaf extract of Daphne mezereum as a novel dye removing material." *Applied Physics A* 124 (2018): 1-7.
22. Seifan, Mostafa, et al. "Amine-modified magnetic iron oxide nanoparticle as a promising carrier for application in bio self-healing concrete." *Applied microbiology and biotechnology* 102 (2018): 175-184.
23. Kashyap, Ajay K., and Tripti Agarwal. "Removal of salicylic acid from aqueous solutions by magnetic biosorbent synthesized from pineapple peel." *The pharma innovation journal* 8 (2019): 502-504.

24. Da'na, Enshirah, Amel Taha, and Eman Afkar. "Green synthesis of iron nanoparticles by Acacia nilotica pods extract and its catalytic, adsorption, and antibacterial activities." *Applied Sciences* 8.10 (2018): 1922.
25. Sahu, S. K., et al. *Determination of uranium in ground water using different analytical techniques*. No. BARC--2014/E/011. Bhabha Atomic Research Centre, Mumbai (India), 2014.
26. Pandey, Pritee, Madhurima Pandey, and Piyush Kant Pandey. "Uranium contamination removal from water by an orchid (Vanda tessellata) based biosorbent." *Journal of Radioanalytical and Nuclear Chemistry* 328.1 (2021): 89-101.
27. Wang, Jianlong, and Shuting Zhuang. "Extraction and adsorption of U (VI) from aqueous solution using affinity ligand-based technologies: an overview." *Reviews in Environmental Science and Bio/Technology* 18.3 (2019): 437-452.
28. Bellamy, L. "The Infra-Red Spectra of Complex Molecules, Springer, Netherlands." (1975): 405-410.
29. Adeogun, Abideen Idowu, et al. "Magnetic tuned sorghum husk biosorbent for effective removal of cationic dyes from aqueous solution: isotherm, kinetics, thermodynamics and optimization studies." *Applied Water Science* 9.7 (2019): 160.
30. Cheng, Yanxia, et al. "A novel freeze-dried natural microalga powder for highly efficient removal of uranium from wastewater." *Chemosphere* 282 (2021): 131084.
31. Xiao-teng, Zhang, et al. "Adsorption of uranium (VI) from aqueous solution by modified rice stem." *Journal of Chemistry* 2019.1 (2019): 6409504.
32. Wang, Xiao, et al. "Studies on adsorption of uranium (VI) from aqueous solution by wheat straw." *Environmental progress & sustainable energy* 31.4 (2012): 566-576.
33. Vasantharaj, Seerangaraj, et al. "Biosynthesis of iron oxide nanoparticles using leaf extract of Ruellia tuberosa: antimicrobial properties and their applications in photocatalytic degradation." *Journal of Photochemistry and Photobiology B: Biology* 192 (2019): 74-82.
34. Yi, Zheng-ji, et al. "Biosorption characteristics of Ceratophyllum demersum biomass for removal of uranium (VI) from an aqueous solution." *Journal of Radioanalytical and Nuclear Chemistry* 313 (2017): 19-27.
35. Ding, Hanlin, et al. "Biosorption of U (VI) by active and inactive Aspergillus niger: equilibrium, kinetic, thermodynamic and mechanistic analyses." *Journal of Radioanalytical and Nuclear Chemistry* 319 (2019): 1261-1275.
36. Rathinam, Aravindhan, et al. "Biosorption of cadmium metal ion from simulated wastewaters using Hypnea valentiae biomass: A kinetic and thermodynamic study." *Bioresource technology* 101.5 (2010): 1466-1470.
37. Sana, Solat, Reza Roostaazad, and Soheila Yaghmaei. "Biosorption of uranium (VI) from aqueous solution by pretreated Aspergillus niger using sodium hydroxide." (2015): 65-74.
38. Sirry, Shadia M., et al. "Chemically treated date stones for uranium (VI) uptake and extraction in aqueous solutions." *Journal of Molecular Liquids* 273 (2019): 192-202.
39. Saleem, Nazia, and Haq Nawaz Bhatti. "Adsorptive removal and recovery of U (VI) by citrus waste biomass." *Bioresources* 6.3 (2011): 2522-38.
40. Akl, Zeinab F. "Theoretical and experimental studies on uranium (vi) adsorption using phosphine oxide-coated magnetic nanoadsorbent." *RSC advances* 11.62 (2021): 39233-39244.
41. Kumar, Nadavala Siva, H. Man, and Heung-Sik Woo. "Biosorption of phenolic compounds from aqueous solutions using pine (Pinus densiflora Sieb) bark powder." *BioResources* 9.3 (2014): 5155-5174.

42. Yuvaraja, Gutha, et al. "Removal of U (VI) from aqueous and polluted water solutions using magnetic Arachis hypogaea leaves powder impregnated into chitosan macromolecule." *International Journal of Biological Macromolecules* 148 (2020): 887-897.
43. Xiao-teng, Zhang, et al. "Adsorption of uranium (VI) from aqueous solution by modified rice stem." *Journal of Chemistry* 2019.1 (2019): 6409504.
44. Kuncham, Kuntaiah, et al. "Efficient removal of uranium (VI) from aqueous medium using ceria nanocrystals: an adsorption behavioural study." *Journal of Radioanalytical and Nuclear Chemistry* 313 (2017): 101-112.
45. Nuhanović, Mirza, et al. "Efficient removal of U (VI) from aqueous solution using the biocomposite based on sugar beet pulp and pomelo peel." *Journal of radioanalytical and nuclear chemistry* 328 (2021): 347-358.
46. Šabanović, Elma, et al. "Biosorption of uranium (VI) from aqueous solution by Citrus limon peels: kinetics, equlibrium and batch studies." *Journal of Radioanalytical and Nuclear Chemistry* 319 (2019): 425-435.
47. Lagergren, Stan. "Zur theorie der sogenannten adsorption geloster stoffe." *Kungliga svenska vetenskapsakademiens. Handlingar* 24 (1898): 1-39.
48. Ho, Yuh-Shan, and Gordon McKay. "Pseudo-second order model for sorption processes." *Process biochemistry* 34.5 (1999): 451-465.
49. Weber Jr, Walter J., and J. Carrell Morris. "Kinetics of adsorption on carbon from solution." *Journal of the sanitary engineering division* 89.2 (1963): 31-59.

Funding declaration

No funding was received for conducting this study.